

Detecting radio afterglows of gamma-ray bursts with FAST *

Zhi-Bin Zhang¹, Si-Wei Kong², Yong-Feng Huang³, Di Li⁴ and Long-Biao Li¹

¹ Department of Physics, College of Sciences, Guizhou University, Guiyang 550025, China; sci.zbzhang@gzu.edu.cn

² Key Laboratory for Particle Astrophysics, Institute of High Energy Physics, Chinese Academy of Sciences, Beijing 100049, China

³ Department of Astronomy, Nanjing University, Nanjing 210093, China; hyf@nju.edu.cn

⁴ National Astronomical Observatories, Chinese Academy of Sciences, Beijing 100012, China

Received 2014 February 24; accepted 2014 May 27

Abstract Using the generic hydrodynamic model of gamma-ray burst (GRB) afterglows, we calculate the radio afterglow light curves of low luminosity, high luminosity, failed and standard GRBs in different observational bands of FAST's energy window. The GRBs are assumed to be located at different distances from us. Our results rank the detectability of GRBs in descending order as high luminosity, standard, failed and low luminosity GRBs. We predict that almost all types of radio afterglows except those of low luminosity GRBs could be observed by a large radio telescope as long as the domains of time and frequency are appropriate. It is important to note that FAST can detect relatively weak radio afterglows at a higher frequency of 2.5 GHz for very high redshift up to $z = 15$ or even more. Radio afterglows of low luminosity GRBs can only be detected after the completion of the second phase of FAST. FAST is expected to significantly expand the sample of GRB radio afterglows in the near future.

Key words: gamma rays: bursts — methods: numerical — telescopes

1 INTRODUCTION

With rapid developments in space and ground telescopes, studies of gamma-ray bursts (GRBs) have come into an era where full wavelength observations are possible (e.g., Gehrels & Razzaque 2013). In particular, with recent space missions such as the *Swift* satellite, the rapid response together with accurate localization enables more detailed follow-up observations by ground-based facilities at longer times and lower frequencies. This has led to a deeper understanding of the physical origins of GRBs. In addition, statistical analysis becomes possible and it is very helpful to compare the properties of GRBs with their afterglows (Sakamoto et al. 2011). Prompt γ -rays and their follow-up X-ray and optical afterglows are found to be correlated with each other, more or less, for both short and long-duration bursts (Gehrels et al. 2008; Nysewander et al. 2009; Kann et al. 2011). It is interesting that Chandra & Frail (2012) found the detectability of radio afterglows to be statistically neither correlated with their γ -ray fluences nor X-ray fluxes, but only with optical brightness. However, observational constraints of radio afterglows are relatively insufficient, although some authors have

* Supported by the National Natural Science Foundation of China.

recently compiled larger datasets (de Ugarte Postigo et al. 2012; Chandra & Frail 2012; Ghirlanda et al. 2013; Staley et al. 2013) since the first radio afterglow of GRB 970508 was discovered (Frail et al. 1997). We need to separately synthesize the GRBs and their afterglows at multiple energy bands and then combine them to explore their comprehensive physics.

In the framework of the fireball internal-external shock model, GRBs are produced when the kinetic energy of an ultra-relativistic flow is dissipated by internal collisions, while the afterglows are emitted when the flow is slowed down by external shocks colliding with matter surrounding the burst. The fireball model has provided numerous successful predictions on GRB afterglows, such as the afterglow itself, jet break in the light curve of afterglows, the optical flash and the afterglow shallow-decay phenomenon, etc. (see Lu et al. 2004; Piran 2004; Zhang 2007 and Gao et al. 2013 for a review). Huang et al. (1999, 2000b) proposed a set of simplified dynamical equations that is consistent with the self-similar solution of Blandford & McKee (1976) in the ultra-relativistic phase, that also agree with the Sedov solution (Sedov 1959) in the non-relativistic phase. Therefore, these equations can conveniently describe GRB afterglows at all post-burst times. For instance, the beaming effects (Rhoads 1997, 1999; Huang et al. 2000c), the rebrightening at multiple-wavelengths (Huang et al. 2004; Xu & Huang 2010; Kong et al. 2010; Yu & Huang 2013) and modeling the multi-band afterglow (Huang et al. 2000c; Huang et al. 2002; Huang & Cheng 2003; Wang et al. 2009; Kong et al. 2009) can be easily dealt with by these equations.

The Square Kilometer Array (SKA) will be the largest and most sensitive configuration of a radio telescope in the world. The SKA project is designed to be constructed via two phases and will receive radio signals at a frequency range from 70 MHz to 10 GHz. In addition, the Five-hundred-meter Aperture Spherical radio Telescope (FAST, Nan et al. 2011; Li et al. 2013) is a Chinese mega-science project that is being built in Guizhou province, located in southwestern China. It will be the largest single-dish radio telescope in the world with an expected first light in September of 2016. FAST will cover the entire spectrum of radio frequencies between 70 MHz and 3 GHz. A possible extension to 8 GHz is being considered in the second phase of FAST. FAST will be equipped with a variety of instruments and has been designed for different scientific purposes including the radio afterglows of GRBs. According to the current data sets presented by Chandra & Frail (2012), the detection rate of radio afterglows is 30%, in which more than half of the radio flux measurements are made at 8.5 GHz. However, nearly 10% of the detected radio afterglows are from bright long GRBs (Ghirlanda et al. 2013; Salvaterra et al. 2012). The reason is that the low-frequency observations could be more affected by the bias of receivers.

In this work, we apply the fireball model to calculate a variety of numerical afterglow curves with changing redshifts for different cases representing failed, low luminosity, high luminosity and standard GRBs. These theoretical light curves based on diverse physical considerations are directly compared with FAST's sensitivity in order to diagnose the detectability by FAST. Our radio light curves within FAST's window are derived for both low (70 MHz–0.5 GHz) and medium/high frequencies (0.5–3 GHz). The structure of our paper is as follows. First, we provide an overview of the observations of GRB radio afterglows in Section 2. A theoretical dynamical model of afterglows and the sensitivity of FAST are introduced in Section 3. Numerical results are shown in Section 4 and we end with a discussion and brief conclusions in Section 5.

2 OVERVIEW OF RADIO AFTERGLOW OBSERVATIONS

Recently, Chandra & Frail (2012) presented a large sample of GRB radio observations covering a 14-year period starting in 1997. Despite the 304 radio afterglows consisting of 2995 flux measurements, only 95 out of 304 were reported to have radio afterglows detected by VLA, corresponding to a detection rate of $\sim 30\%$, of which 1539 measurements were made in 8.5 GHz. They pointed out that the current detection rate of radio afterglows, much lower than in the X-ray (90%) or optical (75%) bands in the *Swift* era, may be seriously limited by instrumental sensitivity. Hancock et al.

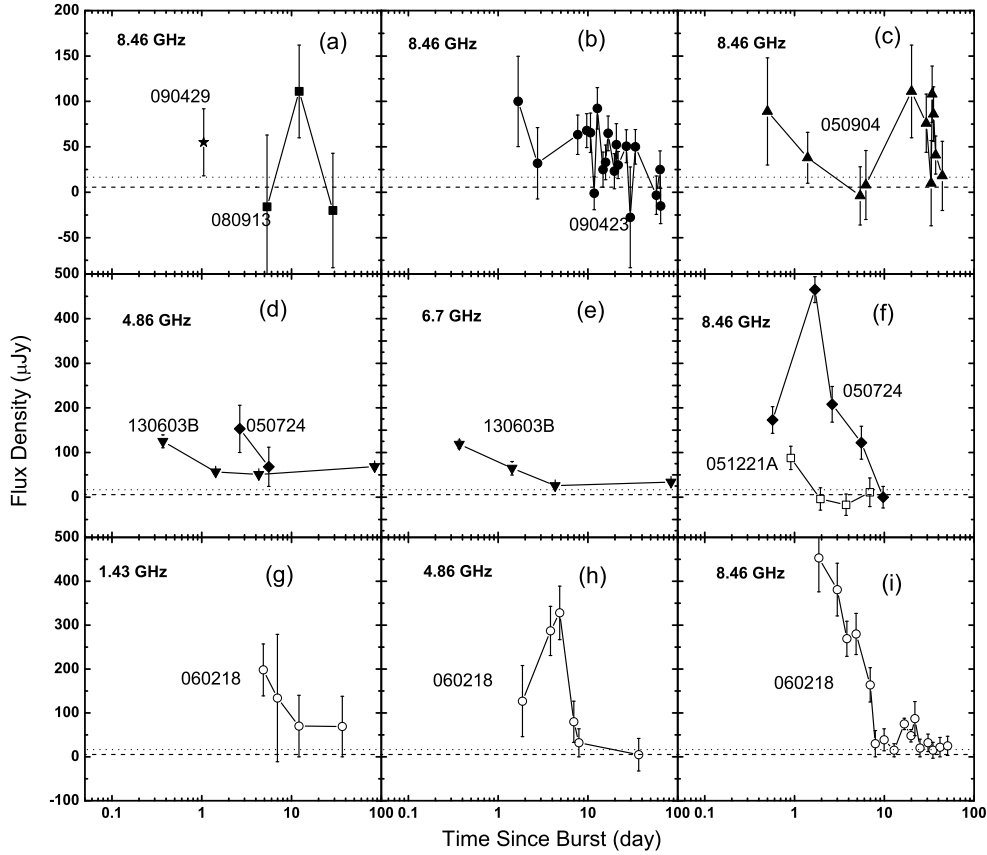


Fig. 1 Broadband radio afterglows of high-redshift bursts (*star*: GRB 090429B; *filled-squares*: GRB 080913; *filled-circles*: GRB 090423; *filled-triangles*: GRB 050904) in panels (a)–(c), short bursts (*filled-triangles*: GRB 130603B; *filled-diamonds*: GRB 050724; *empty squares*: GRB 051221A) in panels (d)–(f) and SNe-associated bursts (*empty circles*: GRB 060218) in panels (g)–(i). The dotted and dashed lines respectively represent the 3σ and 1σ sensitivity limit of FAST in an integration time of 10 min. Note that the data of GRB 130603B are taken from Fong et al. (2014) and all the other radio data are collected from <http://heasarc.gsfc.nasa.gov/W3Browse/all/rssgrbag.html> (Chandra & Frail 2012) directly.

(2013) argued that the lower rate would be caused by two intrinsically different types of bursts, namely radio bright and radio faint sources. However, radio emissions from host galaxies of GRBs also make the radio afterglows more difficult to detect (e.g., Berger et al. 2001; Berger 2013; Li et al. 2014, in preparation). The Chandra & Frail sample contains 33 short-hard bursts, 19 X-ray flashes and 26 GRBs/SNe candidates, including low luminosity bursts and 4 high-redshift bursts, of which only a few radio afterglows are available owing to their lower detection rate. In general, short bursts with smaller isotropic energy, similar to low luminosity ones, are thought to occur in the relatively nearby universe like supernovae. On the other hand, afterglows of short bursts are usually much dimmer than those of long ones (see e.g., Rowlinson 2013 for a review). This motivates us to focus on contrasting the radio afterglows in Figure 1 between short GRBs (050724, 051221A and 130603B), low luminosity GRBs (060218) and high-redshift GRBs (050904, 080913, 090423 and 090429B) with successful detections. Note that only GRB 130603B was not included in Chandra & Frail (2012) and its data are taken from Fong et al. (2014). As the largest next-generation single dish

radio telescope, FAST is expected to bring us many important findings (Nan et al. 2011; Li et al. 2013). The upper limits on flux for FAST (see below) that can be applied to detecting these kinds of bursts are also given in Figure 1, showing that radio afterglows of the above-mentioned three kinds of special bursts would be easily detected by FAST. Interestingly, it is noted that high-redshift bursts, similar to short bursts except for GRB 050724, have a typical flux density of less than 150 μJy in the radio band. Considering the above situations, we will simulate theoretical radio afterglows of different types of bursts and subsequently probe their detectability with FAST.

3 DYNAMICAL MODEL AND FAST SENSITIVITY

In terms of the generic dynamical model (Huang et al. 1999, 2000a,c), the overall evolution of the ejected outflows in both the ultra-relativistic and non-relativistic (Newtonian) phases can generally be described as

$$\frac{dR}{dt} = \beta c \gamma (\gamma + \sqrt{\gamma^2 - 1}), \quad (1)$$

$$\frac{dm}{dR} = 2\pi(1 - \cos\theta)R^2 n m_p, \quad (2)$$

$$\frac{d\theta}{dt} = \frac{c_s}{R} (\gamma + \sqrt{\gamma^2 - 1}), \quad (3)$$

$$\frac{d\gamma}{dm} = -\frac{\gamma^2 - 1}{M_{\text{ej}} + \varepsilon m + 2(1 - \varepsilon)\gamma m}, \quad (4)$$

where R is the radial distance measured in the source frame from the initiation point; m is the rest mass of the swept-up circumburst medium; θ is the half-opening angle of the ejecta; γ is the bulk Lorentz factor of the moving material; t is the arrival time of photons measured in the observer frame; $\beta = \sqrt{1 - \gamma^{-2}}$ and c is the speed of light. n is the number density of the interstellar medium; ε is the general radiative efficiency and would evolve from 1 (high radiative case) to 0 (adiabatic case) within several hours after a burst; M_{ej} is the initial rest mass of the ejecta. c_s is the comoving sound speed determined by $c_s^2 = \hat{\gamma}(\hat{\gamma} - 1)(\gamma - 1)c^2/[1 + \hat{\gamma}(\gamma - 1)]$ with the adiabatic index $\hat{\gamma} = 4/3$ in the ultra-relativistic limit and $\hat{\gamma} = 1$ in the Newtonian limit (Huang et al. 2000b). We further define ξ_e and ξ_B^2 as factors coming from the equipartition of energy for electrons and the comoving magnetic field, respectively.

Denoting Θ as the viewing angle between the velocity of ejecta and the line of sight and $\mu = \cos\Theta$, in the burst comoving frame, we can obtain the synchrotron radiation power of electrons at frequency ν' as (Rybicki & Lightman 1979)

$$P'(\nu') = \frac{\sqrt{3}e^3 B'}{m_e c^2} \int_{\min(\gamma_{e,\min}, \gamma_c)}^{\gamma_{e,\max}} \left(\frac{dN_e'}{d\gamma_e} \right) F\left(\frac{\nu'}{\nu_c'}\right) d\gamma_e, \quad (5)$$

in which $dN_e'/d\gamma_e \propto (\gamma_e - 1)^{-p}$, with the typical value of the electron distribution index p being between 2 and 3 (Huang & Cheng 2003); $\nu_c' = 3\gamma_e^2 e B' (4\pi m_e c)^{-1}$ is the characteristic frequency of electrons with charge e ; $\gamma_c = 6\pi m_e c / (\sigma_T \gamma B'^2 t)$ is the typical Lorentz factor of electrons that cool rapidly due to synchrotron radiation, with σ_T being the Thompson cross-section; $\gamma_{e,\min} = \xi_e(\gamma - 1)m_p(p - 2)/[m_e(p - 1)] + 1$ and $\gamma_{e,\max} \simeq 10^8 (B'/1G)^{-1/2}$ are respectively the minimum and maximum Lorentz factors of electrons, and $F(x) = x \int_x^{+\infty} K_{5/3}(x') dx'$ of which $K_{5/3}(x')$ is the Bessel function. Owing to cosmological expansion, the observed frequency ν should be (Wang et al. 2009)

$$\nu = [\gamma(1 - \beta\mu)]^{-1} \nu' / (1 + z) = \delta \nu' / (1 + z), \quad (6)$$

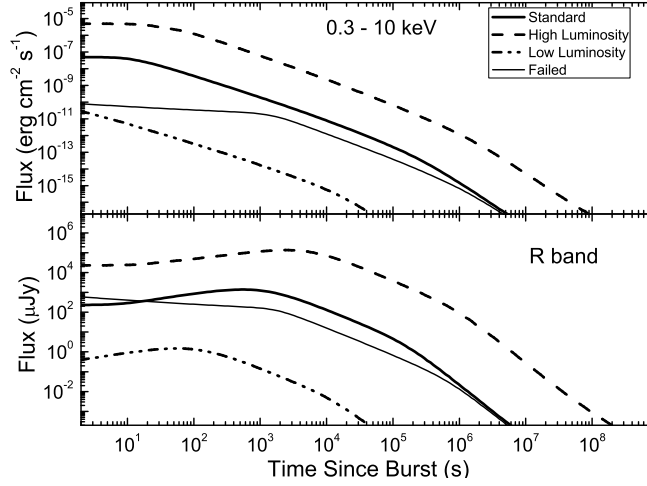


Fig. 2 Plots of afterglow light curves for the standard (*thick solid line*), high luminosity (*dashed line*), low luminosity (*dash-dot-dotted line*) and failed (*thin solid line*) GRBs at the X-ray band (0.3–10 keV) in the upper panel and the optical *R* band in the lower panel for a typical redshift $z = 0.5$ and density $n = 1 \text{ cm}^{-3}$. See the text for more details.

where $\delta = [\gamma(1-\beta\mu)]^{-1}$ is the Doppler factor. For low-frequency radiation, the effect of synchrotron self-absorption on observation should be considered and hence the observed flux density radiated from a cosmological point source would be (Huang et al. 2000b; Wang et al. 2009)

$$F_\nu(t) = \frac{(1+z)\delta^3}{4\pi D_L^2} f(\tau) P'[(1+z)\nu/\delta], \quad (7)$$

where D_L is the luminosity distance and $f(\tau) = (1 - e^{-\tau})/\tau$ is a reduction factor of synchrotron self-absorption with an optical depth τ . In order to calculate the total observed flux densities, we should integrate Equation (7) over the equal arrival time surface determined by

$$t = (1+z) \int \frac{1-\beta\mu}{\beta c} = \text{const}, \quad (8)$$

within the jet boundaries.

Basically, the above model can give a good description for the external shocks and GRB afterglows. For example, the dynamical model has been applied to many GRBs and can explain the observations well (Huang et al. 2006; Kong et al. 2009; Xu et al. 2009; Kong et al. 2010; Xu et al. 2011; Yu & Huang 2013; Geng et al. 2013). Here in Figure 2, we display some examples of afterglow light curves at the X-ray band (0.3–10 keV) and the optical *R*-band calculated using this model. It can be seen that this model basically matches the general behaviors of multi-band afterglows (e.g., Zhang et al. 2006; Nousek et al. 2006; Zhang et al. 2007a; Liang et al. 2008; Troja et al. 2007). Moreover, afterglows from extreme GRBs, such as high luminosity, low luminosity and failed bursts, are also predicted to provide new opportunities with observations that will be made by FAST.

Table 1 Parameters describing the Nine Sets of Receivers that are Part of FAST

No.	Band [†] (GHz)	ν_c^\dagger (GHz)	$\Delta\nu^\dagger$ (MHz)	T_{sys}^\dagger (K)	$F_{\text{lim},1}$ (μJy)	$F_{\text{lim},2}$ (μJy)	$F_{\text{lim},3}$ (μJy)	T'_{sys} (K)	$F'_{\text{lim},1}$ (μJy)	$F'_{\text{lim},2}$ (μJy)	$F'_{\text{lim},3}$ (μJy)
1	0.07–0.14	0.1	70	1000	293.6	168.7	119.4	140	41.0	23.5	16.9
2	0.14–0.28	0.2	140	400	82.5	47.6	33.8	140	28.8	16.6	11.9
3	0.28–0.56	0.4	280	150	21.9	12.7	8.9	130	19.1	11.1	7.8
4	0.56–1.02	0.8	560	60	6.1	3.6	2.5	97	9.9	5.8	4.2
5	0.32–0.334	0.328	14	200	130.7	75.3	53.5	125	81.7	47.1	33.2
6	0.55–0.64	0.6	90	60	15.5	8.9	6.4	112	28.9	16.6	11.9
7	1.15–1.72	1.45	550	25	2.5	1.4	1.1	61	6.3	3.6	2.5
8	1.23–1.53	1.38	300	25	3.6	1.9	1.4	60	8.6	5.0	3.6
9	2.00–3.00	2.5	1000	25	1.9	1.1	0.8	30	2.2	1.4	0.8

[†] These data are taken from Nan et al. (2011). $F_{\text{lim},i}$ ($i = 1, 2, 3$) denotes the limiting flux densities for different integration times $\Delta\tau$ of 10, 30 and 60 min. The limited flux densities $F'_{\text{lim},i}$ ($i = 1, 2, 3$) are estimated in terms of the system temperatures given by VLA's template (<https://science.nrao.edu/facilities/vla>) within the above corresponding time levels.

In order to explore the detectability of FAST, here we adopt the following sensitivity to estimate the RMS noise in a position-switching observing mode as

$$F_{\text{lim}} = \frac{(S/N)2K_b T_{\text{sys}}}{A_e \sqrt{\Delta\tau \Delta\nu}} \simeq (12 \mu\text{Jy}) \left(\frac{0.77 \times 10^3 \text{m}^2/\text{K}}{A_e/T_{\text{sys}}} \right) \left(\frac{S/N}{3} \right) \left(\frac{1 \text{h}}{\Delta\tau} \right)^{1/2} \left(\frac{100 \text{MHz}}{\Delta\nu} \right)^{1/2}, \quad (9)$$

where A_e is the effective area defined by $A_e = \eta_A A_g$ with an aperture efficiency of $\eta_A = 0.65$ (Yue et al. 2014, in preparation), $\Delta\tau$ and $\Delta\nu$ are respectively the bandwidth and the integration time, the illuminated geometric area is $A_g = \pi \times (300/2)^2 \text{m}^2$ and the system temperature of FAST is T_{sys} .

Table 1 displays parameters describing the predicted performance of FAST at different frequencies. S/N stands for the signal-to-noise ratio and is generally taken as being no less than 3. More detailed properties of FAST can be found in Nan et al. (2011). Note that we have calculated parameters describing FAST by assuming that its behavior in terms of temperature is similar to receivers that are part of VLA. We acknowledge the difficulty in performing a bandpass calibration for a single dish, which is more difficult than that for interferometers. The detection of a faint, broadband continuum signal, however, has been achieved by single dishes before. The FAST project is also looking into new calibration technologies, such as injecting an artificial flat spectrum signal into its optical path.

4 RESULTS

To determine the sensitivity of FAST to GRB radio afterglows, we have chosen the cases of standard, high-luminosity, low-luminosity and failed GRBs for a comparative study. For convenience, let us define the initial values or parameters of these bursts as follows. (1) Standard GRBs: initial isotropic energy $E_0 = 10^{52}$ erg and $\gamma_0 = 300$. (2) High luminosity GRBs: $E_0 = 10^{54}$ erg and $\gamma_0 = 300$. (3) Low luminosity GRBs: $E_0 = 10^{49}$ erg and $\gamma_0 = 300$. (4) Failed GRBs: $E_0 = 10^{52}$ erg and $\gamma_0 = 30$. Apart from these differences, we assume all the bursts have the same values for the other parameters, namely $n = 1 \text{cm}^{-3}$, $p = 2.5$, $\xi_e = 0.1$, $\xi_B^2 = 0.001$, $\theta = 0.1$ and $\Theta = 0$ throughout this paper. Also, an assumption about the radiative efficiency $\varepsilon = 0$ has been made because the relativistic fireball becomes fully adiabatic within several hours after a burst. Light curves of radio afterglows at different redshifts, i.e. $z = 0.5, 1, 5, 10$ and 15 , have been derived in order to study FAST's capability of probing bursts in the early universe.

4.1 Light Curves of Radio Afterglows in the FAST Window

Figures 3–7 show that almost all radio afterglow light curves, except failed GRB afterglows, have the same general characteristics of slow rise and fast decay although they may have distinct physical origins. We also find a common and interesting phenomenon that with the increase of observing frequency, the light curve peaks earlier, and the peak flux is also higher. At the same time, radio afterglows of the standard and failed GRBs have almost the same peak time and the same peak flux density due to their similar kinetic energies. The two kinds of bursts decay congruently after their peak times. At higher frequencies and larger redshifts, the peak flux densities of failed GRBs are slightly weaker than those of the standard ones. Both the peak flux density and the peak time of radio afterglows sensitively depend on the initial energy injection. For failed GRBs, the rising part is largely affected by the small initial Lorentz factors of the ejecta from the central engine. In any case, we notice that the radio afterglows of the low luminosity GRBs have the lowest brightness except that they are stronger than those of the failed GRBs at an early stage of less than 1 h. The intersection point would be postponed when the observing frequency is relatively lower for a farther burst. Note that it seems unlikely that FAST can detect any kind of radio afterglow emission at the extremely low frequency of ≤ 0.1 GHz. The radio flux density at higher frequency but the same distance or redshift is usually stronger than that at lower frequency when they are observed at the same time and can be detected at a very early stage. Furthermore, it is found that the radio flux densities are relatively insensitive to redshift as seen in Figures 5–7, which is consistent with previous investigations (e.g., Ciardi & Loeb 2000; Gou et al. 2004; Frail et al. 2006; Chandra & Frail 2012).

4.1.1 Standard GRBs

The thick solid lines in Figures 3–7 denote the case of a standard fireball in different energy bands and redshifts. For the redshift $z = 0.5$, the radio emissions that peak at $\nu > 0.4$ GHz can be easily detected by FAST. With the increase of observing frequency, the bursts gradually brighten. FAST can even detect very early radio afterglows in the prompt phase for a time of less than 10 s at 2.5 GHz. It is interesting that in high frequency bands, the radio afterglow can typically be observable for ~ 115 d. The peak flux densities at 1.4 GHz and 2.5 GHz can reach 70 μJy and 200 μJy , respectively. For the redshift $z = 1$, FAST can detect the radio emission in the frequency band of $\nu > 0.6$ GHz, especially $\nu = 2.5$ GHz from 20 s to 62 d after a burst with an integration time of 1 h. The earliest detection time may start as early as 10 s. For the redshift $z = 5$, radio afterglows under 0.8 GHz are undetectable by FAST. The peak flux densities at 0.8 GHz and 2.5 GHz can respectively reach 3 μJy and 6 μJy , which will be observed up to 52 d from the earliest starting time of 30 min. For much higher redshifts of $z = 10$ and 15, the radio flux densities have a peak value of ~ 2 μJy and only radio afterglows above 1.4 GHz can be marginally detected. Note that the GRB radio afterglows in the standard case usually peak at 10–100 d, which is consistent with the observations described in Chandra & Frail (2012).

4.1.2 High luminosity GRBs

The high luminosity GRBs marked with thick dashed lines in Figures 3–7 are driven by the largest energy ejection and their radio afterglows naturally radiate the strongest brightness when they are located at a given distance. For nearby bursts with a redshift of $z = 0.5$, FAST has the capability of detecting all radio afterglows at a frequency of no less than 100 MHz. The typical peak flux densities are 100 μJy at 0.2 GHz and 7×10^3 μJy at 2.5 GHz. The former can be detected from 3 d to 3.5 yr and the latter can be observed from several seconds to 9 yr after the burst. For a redshift of $z = 1$, FAST could detect the weak peak flux in a post-burst time of 2 h to 1200 d in channel 3 at 0.4 GHz and 30 s to 6 yr at a frequency of $\nu = 1.4$ GHz. The radio afterglow flux densities for redshifts higher

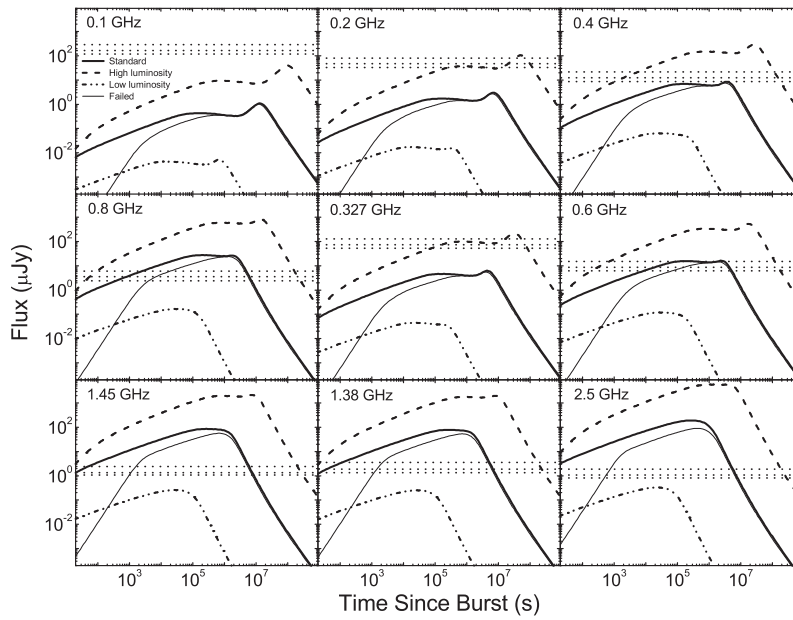


Fig. 3 Radio flux density of GRBs at a redshift $z = 0.5$ versus observation time t in the observer frame at various frequencies within FAST's window. The radio light curves of standard, high-luminosity, low-luminosity and failed GRBs are marked with thick solid, dashed, dash-dot-dotted and thin solid lines, respectively, and are displayed in the top-left panel. Three horizontal dotted lines from top to bottom represent 1σ ($S/N=1$) limiting flux density of FAST for 10, 30 and 60 min integration times respectively. See the text for details.

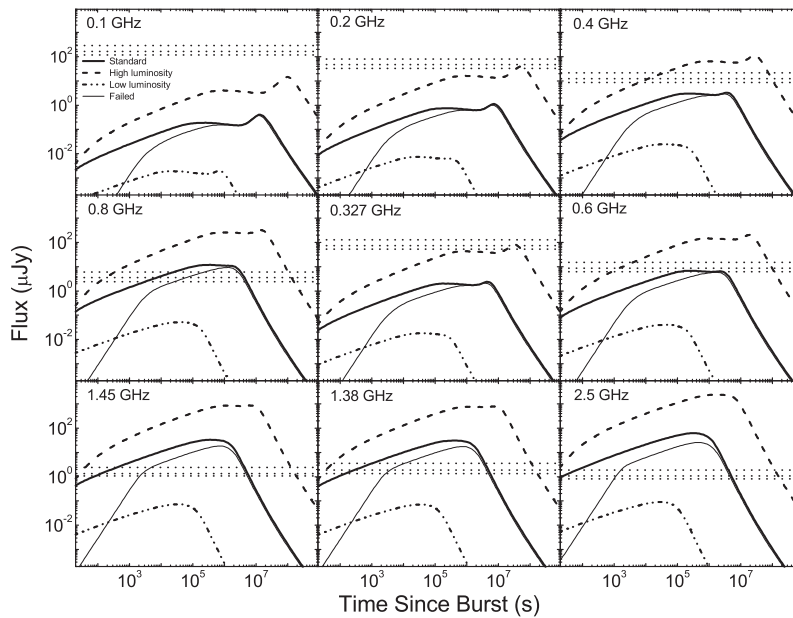


Fig. 4 Radio flux density of GRBs at a redshift $z = 1$ versus observation time t in the observer frame at various frequencies within FAST's window. The line styles are the same as in Fig. 3.

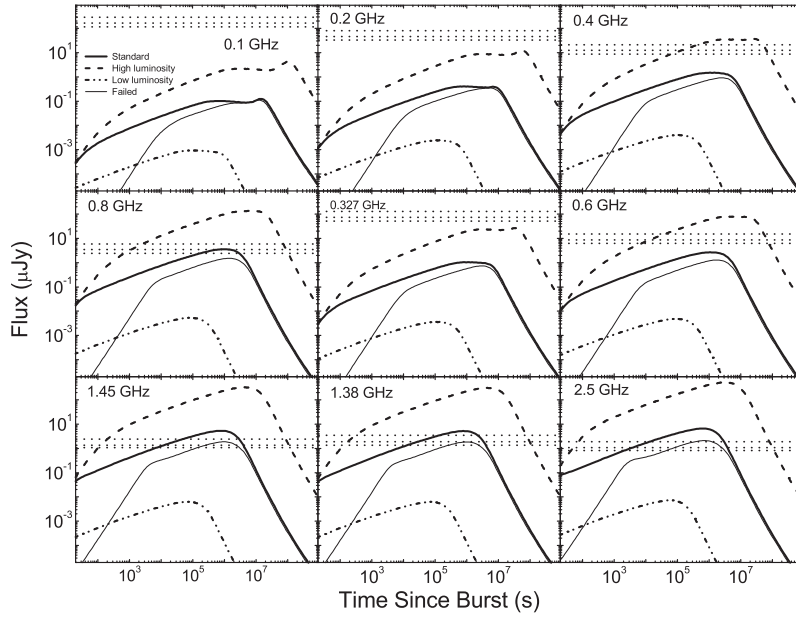


Fig. 5 Radio flux density of GRBs at a redshift $z = 5$ versus observation time t in the observer frame at various frequencies within FAST's window. The line styles are the same as in Fig. 3.

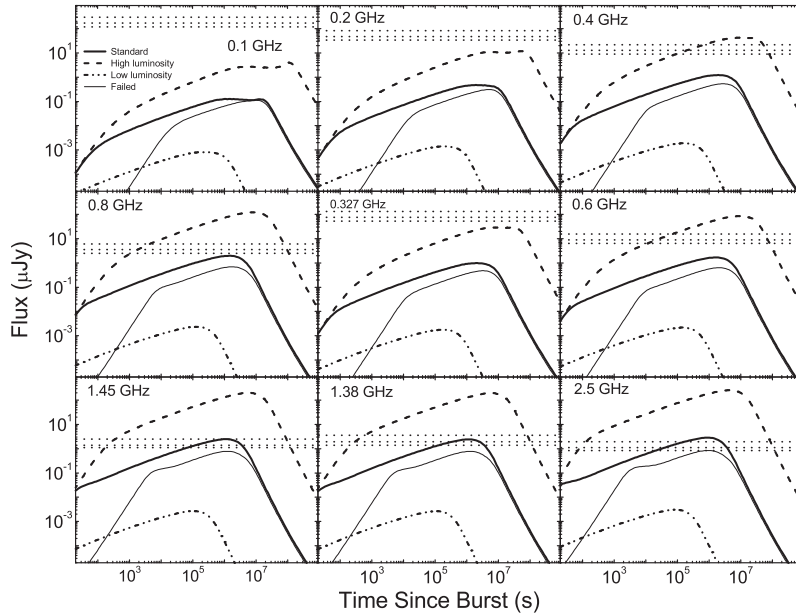


Fig. 6 Radio flux density of GRBs at a redshift $z = 10$ versus observation time t in the observer frame at various frequencies within FAST's window. The line styles are the same as in Fig. 3.

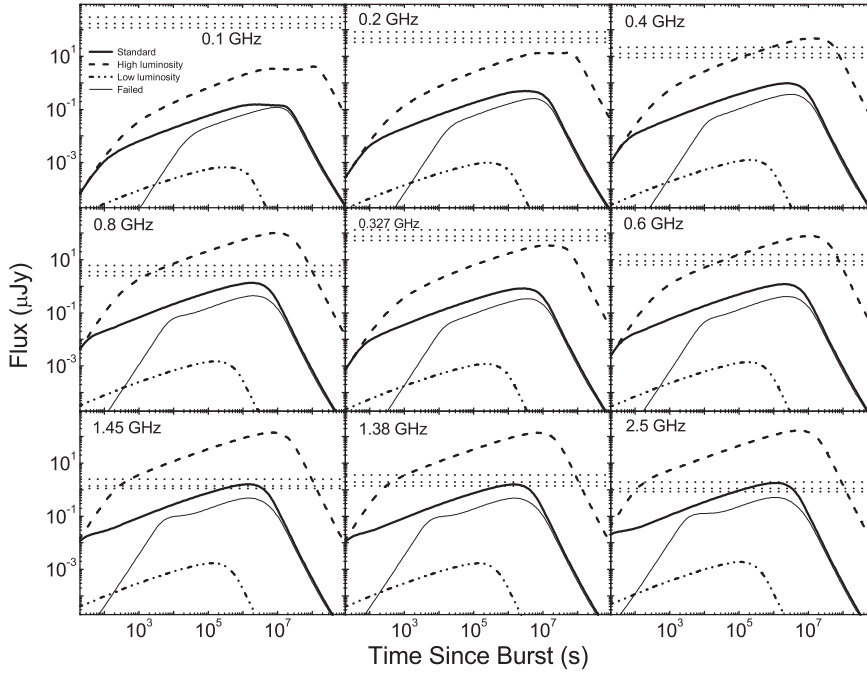


Fig. 7 Radio flux density of GRBs at a redshift $z = 15$ versus observation time t in the observer frame at various frequencies within FAST's window. The line styles are the same as in Fig. 3.

than 5 are undetectable under $\nu \simeq 300$ MHz but can be safely detected from 1 d to 2.5 yr at 0.4 GHz and from several tens of seconds to 4 yr in high frequency bands. The peak radio flux densities at 0.4–2.5 GHz for $z = 15$ can reach 50–200 μJy , which is much higher than the threshold of FAST.

4.1.3 Low luminosity GRBs

In contrast, low luminosity GRBs, denoted by dash-dot-dotted lines in Figures 3–7, consist of some special bursts with lower energy input. This leads to a smaller kinetic energy of outflows and then much weaker radio afterglows peaking at an earlier time, around 1 d after the GRB trigger. The weakest radio brightness is only $\sim 10^{-4}$ μJy at 100 MHz for a redshift $z = 15$. The strongest flux density can approach 0.3 μJy at 2.5 GHz for $z = 0.5$ and is just close to the detection limit of FAST for an integration time of 1 h. It is obvious that FAST can hardly detect radio afterglows from these low luminosity GRBs. In the future, if FAST's passband can be expanded to 8 GHz, low luminosity GRBs could also be detected. We can also consider increasing the integration time to distinguish the radio afterglow from a low level background.

4.1.4 Failed GRBs

Such kinds of bursts are thought to be produced by an isotropic fireball with kinetic energy like that of standard bursts but with much lower Lorentz factors with values of several tens. As shown in Figures 3–7, radio afterglows of failed GRBs and the standard ones peak nearly simultaneously and they decay with time in the same way after the peak time. Compared with standard bursts, radio

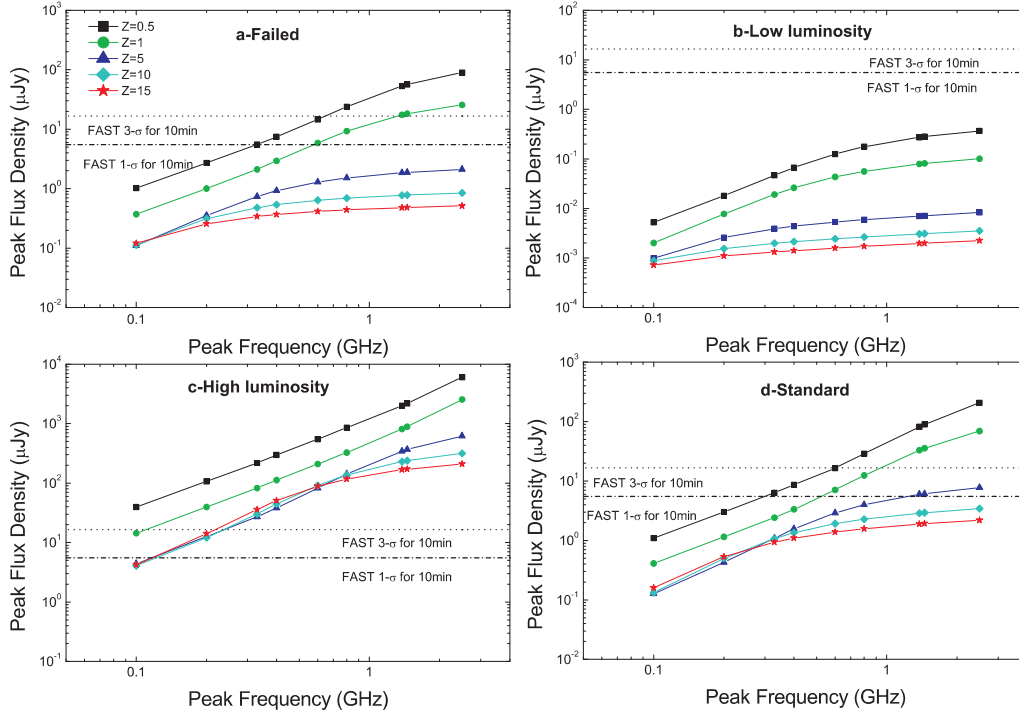


Fig. 8 Peak radio flux density versus peak frequency for the failed, low luminosity, high luminosity and standard GRBs at five representative redshifts. The two horizontal lines on top and bottom respectively stand for the 3σ and 1σ limiting flux density of FAST in a 10 min integration time. The different symbols for various redshifts are given in panel a. Note that a systematic temperature of $T_{\text{sys}}=20\text{ K}$ and a bandwidth of $\Delta\nu = 100\text{ MHz}$, which are typical parameters for FAST, have been used for our estimation here. See the text for details.

afterglows of failed bursts can be detected mainly at later times. For $z = 0.5$, FAST can hardly detect them at a frequency lower than 0.6 GHz at a level of 3σ with a 1 h integration time. However, we can detect the radio afterglows up to 85 d at higher frequencies above 0.8 GHz. The afterglow is observable from a time of 1000, 70, 20, 15 and 8 min for 0.6, 0.8, 1.38, 1.45 and 2.5 GHz after the burst, respectively. For the redshift $z = 1$, only radio emissions at a frequency larger than 0.6 GHz are detectable from 1 d to 60 d. Radio afterglows at a redshift of $z = 5$ for a frequency larger than 1.4 GHz can be observed. The radio flux densities at 0.8, 1.38, 1.45 and 2.5 GHz are at a lower level of 1–2 μJy . For $z > 10$, radio afterglows of the failed GRBs become very difficult to detect by FAST with its current sensitivity using a 1 h integration time.

4.2 Peak Spectra of Radio Afterglows in FAST's Window

To investigate the sensitivity of FAST's receiver at different frequencies, we plot the peak frequency against the peak flux density for the above-mentioned four types of bursts at different redshifts in Figure 8.

The data utilized here are extracted from the above calculations. Radio emission would be steeply cut off by the self-absorption effect at lower frequencies below several GHz. This frequency range covers FAST's frequency bands of 70 MHz–3 GHz, which causes the radio flux density F to

be a power-law function of $F \propto \nu^2$ (e.g., Sari et al. 1998; Wu et al. 2005) if the observation frequency ν is less than the synchrotron self-absorption frequency ν_a . With a systematic temperature of $T_{\text{sys}} = 20$ K, the bandwidth of $\Delta\nu = 100$ MHz and the aperture efficiency of $\eta_A = 0.65$ for FAST, we have plotted the 1σ and 3σ limiting flux density for a 10 min integration time for comparison (see Fig. 8).

We can see from Panel (a) in Figure 8 that radio afterglows of failed bursts are only detectable for nearby sources with redshifts less than 5 and at relatively high frequencies. Panel (b) shows that the radio peaks of low luminosity bursts are far below the detection limits in all our cases and thus are difficult to detect with FAST. By contrast, we see from Panel (c) that the peak flux densities of high luminosity GRBs are always above the detection limits, making them the best candidates for monitoring at almost any redshifts and frequencies except very high redshift at a lower frequency of $\nu < 200$ MHz. Panel (d) displays the radio peaks of the standard GRBs. They can be observed by FAST up to a very high redshift of $z = 10$ at higher frequency, very different from the failed bursts with the relatively lower flux density at the higher frequency, although they exhibit similar observational properties at lower redshifts in all frequency bands of FAST. Another interesting phenomenon is that the radio spectrum evolves with cosmological redshift in the observer frame. In addition, the spectral shape of low luminosity bursts clearly differs from that of other classes of GRBs, which hints that they could have a distinct physical origin.

Recent numerical simulations by a few other authors have shown that sideways expansion, edge effect, even the effect of viewing jets off axis (Zhang et al. 2014a), together with their microphysical process transitioning from an ultra-relativistic to non-relativistic phase could play a significant role in the expected light curves and spectra of afterglows (van Eerten et al. 2010; van Eerten & MacFadyen 2012). However, the results given by the above updated blastwave models do not significantly differ from those predicted by the generic afterglow model utilized in this paper, especially for late-time radio afterglows, of which the peak flux density, the peak time and the post-peak decay are very comparable as a whole. Furthermore, it is worth pointing out that our numerical radio afterglows at 1.43 GHz are fairly consistent with those calculated with the external shock model proposed by Chandra & Frail (2012).

5 DISCUSSION AND CONCLUSIONS

It is interesting to notice that the fractions of high, low and medium isotropic energy GRBs in the pre-*Swift* era are 4%, 16% and 80% respectively (Friedman & Bloom 2005). As *Swift*/BAT is more sensitive to long-soft bursts than pre-*Swift* missions, the percentages are 32%, 3% and 65% respectively for the high, low and medium isotropic energy GRBs in the *Swift* era. Obviously, the fraction of high luminosity GRBs detected by *Swift*/BAT is much larger than that of pre-*Swift* detectors, but the fraction of low luminosity GRBs is just the opposite. Detections by the ongoing *Swift* satellite favors long bursts with higher redshifts on average. This naturally yields progressively more ultra-long bursts observed with duration up to $10^4 - 10^6$ s (Zhang et al. 2014b). How the radio afterglows of these GRBs will behave is a very important problem. We believe that their radio afterglows should be detectable by FAST. It will promote the study of early cosmology especially with the help of future FAST observations. This advantage is mainly attributed to the fact that long GRBs with high-redshifts are generally thought to be produced by higher luminosity sources, e.g. the collapse of very massive stars.

Rhoads (1997) pointed out that γ -ray radiation from some GRBs with jets cannot be observed due to relativistic beaming effects, but the corresponding late time afterglow emission is less beamed and can safely reach us. These lower frequency radiations are called orphan afterglows, since they are not associated with any detectable GRBs. However, Huang et al. (2002) pointed out another possibility that orphan afterglows can also be produced by failed GRBs (or a dirty fireball). They argued that the number of failed GRBs may be much larger than that of normal bursts. It is very difficult

to distinguish the two different origins of orphan afterglows. The initial Lorentz factor of ejecta is a key parameter that, in principle, makes the failed GRBs different from other kinds of bursts. The compactness limit was thought to be a robust method for estimating the initial Lorentz factor (Zou et al. 2011). Unfortunately, current Lorentz factor estimates are still controversial although extensive attempts had been made both theoretically and observationally (e.g., Zhang et al. 2007b, 2011; Li 2010; Liang et al. 2010, 2011; Zou & Piran 2010; Zou et al. 2011; Zhao et al. 2011; Chang et al. 2012; Hascoët et al. 2014). These measured properties are useful for discriminating between failed and standard GRBs from their radio afterglows because such low frequency emission can be observed for quite a long time (Huang et al. 2002). FAST may make an important contribution in this aspect.

Note that the contributions of host galaxies to radio fluxes has been neglected in our numerical calculations for simplification. This effect will add difficulties for afterglow observations with FAST and the detection rate of radio afterglows may be less optimistic than our current study (Li et al. 2014, in preparation). On the other hand, the system temperature T_{sys} is sensitively dependent on a variety of realistic factors and will be measured only after the radio telescope is built. As a single dish antenna, FAST will operate in a lower frequency range, i.e. from 70 MHz to 3 GHz in its first phase, and may be extended to 8 GHz in its second phase. The Low Frequency Array (LOFAR) covers relatively lower observation frequencies of 10–240 MHz (van Haarlem et al. 2013), partly overlapped with that of FAST. Thomson et al. (2007) gave the theoretical equation, $T_{\text{sky}} = 60\lambda^{2.55}$ K, as the estimation of T_{sys} . It has been shown that LOFAR will be dominated by sky noise under 65 MHz, close to FAST's lower frequency limit of 70 MHz. By contrast, at a frequency of 200 MHz, FAST's detection sensitivity is about one order of magnitude higher than LOFAR.

In addition, we stress that the limiting sensitivity of FAST at $\nu > 0.4$ GHz for a 1 h integration time is under 10 μJy , which is much better than EVLA if FAST's instrumental noise is ideally controlled to be below the values adopted in this work. In this case, we predict that FAST will be the most powerful new-generation radio telescope for studying radio afterglows. If FAST is incorporated into an international Very-Long-Baseline Interferometry project, it would have an even more powerful capability at detecting radio emission from low luminosity GRBs or very distant (Chandra et al. 2010) GRBs, which should largely increase the detection rate of radio afterglows in the near future. Considering that GRBs with $E_{\text{iso}} = 10^{51} - 10^{53}$ erg at $z \geq 20$ will be observed by the next generation of instruments in near infrared and radio bands (Mesler et al. 2014), our results will be very valuable for making further survey plans of GRB radio afterglows with upcoming radio telescopes such as FAST, SKA and so on.

We summarize our major conclusions in the following:

- (1) We present a quantitative prediction for the detectability of GRB radio afterglows with FAST, based on the generic dynamical afterglow model. Our calculations are carried out for four kinds of bursts, i.e. failed GRBs, low luminosity GRBs, high luminosity GRBs and standard GRBs. We found that the radio afterglow detection rate sensitively depends on the model parameters of the Lorentz factor and isotropic energy.
- (2) We predict that radio afterglows of all the above types of bursts except the low luminosity ones should be detected by FAST in wide ranges of time, frequency and redshift. The detectabilities decrease in the order defined by high luminosity, standard, failed and low luminosity GRBs.
- (3) FAST is able to detect radio afterglows of GRBs at a redshift up to $z \sim 10$ or even more, which will be very helpful for studies of GRB event rate and GRB cosmology.
- (4) Radio afterglows of low luminosity GRBs will be detectable in the second phase of FAST or if the integration time is extended enough.

Acknowledgements We thank the anonymous referee for their helpful comments and suggestions. We appreciate D. A. Frail and P. Chandra for giving us their invaluable observation data of radio afterglows. We acknowledge R. D. Nan, B. Zhang, X. F. Wu, Y. Z. Fan, C. S. Choi and H. Y. Chang for

their helpful discussions. This work was supported by the National Basic Research Program of China (973 Program, 2014CB845800 and 2012CB821800), the National Natural Science Foundation of China (Grant Nos. 11033002, 11263002, 11473012, U1431126 and 11311140248) and the Guizhou Natural Science Foundation (Grant Nos. 20134021 and 20134005). SWK acknowledges support by the China Postdoctoral Science Foundation under grant 2012M520382.

References

- Berger, E. 2014, *ARA&A*, 52, 43
- Berger, E., Kulkarni, S. R., & Frail, D. A. 2001, *ApJ*, 560, 652
- Blandford, R. D., & McKee, C. F. 1976, *Physics of Fluids*, 19, 1130
- Chandra, P., & Frail, D. A. 2012, *ApJ*, 746, 156
- Chandra, P., Frail, D. A., Fox, D., et al. 2010, *ApJ*, 712, L31
- Chang, Z., Lin, H.-N., & Jiang, Y. 2012, *ApJ*, 759, 129
- Ciardi, B., & Loeb, A. 2000, *ApJ*, 540, 687
- de Ugarte Postigo, A., Lundgren, A., Martín, S., et al. 2012, *A&A*, 538, A44
- Fong, W., Berger, E., Metzger, B. D., et al. 2014, *ApJ*, 780, 118
- Frail, D. A., Cameron, P. B., Kasliwal, M., et al. 2006, *ApJ*, 646, L99
- Frail, D. A., Kulkarni, S. R., Costa, E., et al. 1997, *Nature*, 389, 261
- Friedman, A. S., & Bloom, J. S. 2005, *ApJ*, 627, 1
- Gao, H., Lei, W.-H., Zou, Y.-C., Wu, X.-F., & Zhang, B. 2013, *New Astron. Rev.*, 57, 141
- Gehrels, N., Barthelmy, S. D., Burrows, D. N., et al. 2008, *ApJ*, 689, 1161
- Gehrels, N., & Razzaque, S. 2013, *Frontiers of Physics*, 8, 661
- Geng, J. J., Wu, X. F., Huang, Y. F., & Yu, Y. B. 2013, *ApJ*, 779, 28
- Ghirlanda, G., Salvaterra, R., Burlon, D., et al. 2013, *MNRAS*, 435, 2543
- Gou, L. J., Mészáros, P., Abel, T., & Zhang, B. 2004, *ApJ*, 604, 508
- Hancock, P. J., Gaensler, B. M., & Murphy, T. 2013, *ApJ*, 776, 106
- Hascoët, R., Beloborodov, A. M., Daigne, F., & Mochkovitch, R. 2014, *ApJ*, 782, 5
- Huang, Y. F., Dai, Z. G., & Lu, T. 1999, *MNRAS*, 309, 513
- Huang, Y. F., Dai, Z. G., & Lu, T. 2000a, *MNRAS*, 316, 943
- Huang, Y. F., Gou, L. J., Dai, Z. G., & Lu, T. 2000b, *ApJ*, 543, 90
- Huang, Y. F., Dai, Z. G., & Lu, T. 2000c, *A&A*, 355, L43
- Huang, Y. F., Dai, Z. G., & Lu, T. 2002, *MNRAS*, 332, 735
- Huang, Y. F., & Cheng, K. S. 2003, *MNRAS*, 341, 263
- Huang, Y. F., Wu, X. F., Dai, Z. G., Ma, H. T., & Lu, T. 2004, *ApJ*, 605, 300
- Huang, Y. F., Cheng, K. S., & Gao, T. T. 2006, *ApJ*, 637, 873
- Kann, D. A., Klose, S., Zhang, B., et al. 2011, *ApJ*, 734, 96
- Kong, S., Huang, Y., Cheng, K., & Lu, T. 2009, *Science in China: Physics, Mechanics and Astronomy*, 52, 2047
- Kong, S. W., Wong, A. Y. L., Huang, Y. F., & Cheng, K. S. 2010, *MNRAS*, 402, 409
- Li, D., Nan, R., & Pan, Z. 2013, in *IAU Symposium*, 291, ed. J. van Leeuwen, 325 (arXiv:1210.5785)
- Li, Z. 2010, *ApJ*, 709, 525
- Liang, E.-W., Racusin, J. L., Zhang, B., Zhang, B.-B., & Burrows, D. N. 2008, *ApJ*, 675, 528
- Liang, E.-W., Yi, S.-X., Zhang, J., et al. 2010, *ApJ*, 725, 2209
- Liang, E.-W., Lü, H., Yi, S.-X., et al. 2011, *International Journal of Modern Physics D*, 20, 1955
- Lu, T., Huang, Y. F., Dai, Z. G., & Wei, D. M. 2004, in *Cosmic Gamma-Ray Sources, Astrophysics and Space Science Library*, 304, eds. K. S. Cheng, & G. E. Romero, 225
- Mesler, R. A., Whalen, D. J., Smidt, J., et al. 2014, *ApJ*, 787, 91
- Nan, R., Li, D., Jin, C., et al. 2011, *International Journal of Modern Physics D*, 20, 989

- Nousek, J. A., Kouveliotou, C., Grupe, D., et al. 2006, *ApJ*, 642, 389
- Nysewander, M., Fruchter, A. S., & Pe'er, A. 2009, *ApJ*, 701, 824
- Piran, T. 2004, *Reviews of Modern Physics*, 76, 1143
- Rhoads, J. 1997, *ApJ*, 487, L1
- Rhoads, J. 1999, *ApJ*, 525, 737
- Rowlinson, A. 2013, 7th Huntsville Gamma-Ray Burst Symposium, GRB 2013: paper 22 in eConf Proceedings C1304143, arXiv:1308.1684
- Rybicki, G. B., & Lightman, A. P. 1979, *Radiative Processes in Astrophysics* (New York, Wiley-Interscience)
- Sakamoto, T., Barthelmy, S. D., Baumgartner, W. H., et al. 2011, *ApJS*, 195, 2
- Salvaterra, R., Campana, S., Vergani, S. D., et al. 2012, *ApJ*, 749, 68
- Sari, R., Piran, T., & Narayan, R. 1998, *ApJ*, 497, L17
- Sedov, L. I. 1959, *Similarity and Dimensional Methods in Mechanics* (New York: Academic Press)
- Staley, T. D., Titterton, D. J., Fender, R. P., et al. 2013, *MNRAS*, 428, 3114
- Thompson, A. R., Moran, J. M., & Swenson, G. W., 2007, *Interferometry and Synthesis in Radio Astronomy* (2nd edition, John Wiley & Sons)
- Troja, E., Cusumano, G., O'Brien, P. T., et al. 2007, *ApJ*, 665, 599
- van Eerten, H. J., Leventis, K., Meliani, Z., Wijers, R. A. M. J., & Keppens, R. 2010, *MNRAS*, 403, 300
- van Eerten, H. J., & MacFadyen, A. I. 2012, *ApJ*, 751, 155
- van Haarlem, M. P., Wise, M. W., Gunst, A. W., et al. 2013, *A&A*, 556, A2
- Wang, X., Huang, Y. F., & Kong, S. W. 2009, *A&A*, 505, 1213
- Wu, X. F., Dai, Z. G., Huang, Y. F., & Lu, T. 2005, *ApJ*, 619, 968
- Xu, M., Huang, Y.-F., & Lu, T. 2009, *RAA (Research in Astronomy and Astrophysics)*, 9, 1317
- Xu, M., & Huang, Y. F. 2010, *A&A*, 523, A5
- Xu, M., Nagataki, S., & Huang, Y. F. 2011, *ApJ*, 735, 3
- Yu, Y.-B., & Huang, Y.-F. 2013, *RAA (Research in Astronomy and Astrophysics)*, 13, 662
- Zhang, B., Fan, Y. Z., Dyks, J., et al. 2006, *ApJ*, 642, 354
- Zhang, B. 2007, *ChJAA (Chin. J. Astron. Astrophys.)*, 7, 1
- Zhang, B.-B., Liang, E.-W., & Zhang, B. 2007a, *ApJ*, 666, 1002
- Zhang, B.-B., van Eerten, H., Burrows, D. N., et al. 2014a, arXiv1405.4867
- Zhang, B.-B., Zhang, B., Murase, K., Connaughton, V., & Briggs, M. S. 2014b, *ApJ*, 787, 66
- Zhang, Z. B., Xie, G. Z., Deng, J. G., & Wei, B. T. 2007b, *Astronomische Nachrichten*, 328, 99
- Zhang, Z., Zhao, Y., & Zhang, Y. 2011, *Ap&SS*, 333, 89
- Zhao, X.-H., Li, Z., & Bai, J.-M. 2011, *ApJ*, 726, 89
- Zou, Y.-C., & Piran, T. 2010, *MNRAS*, 402, 1854
- Zou, Y.-C., Fan, Y.-Z., & Piran, T. 2011, *ApJ*, 726, L2